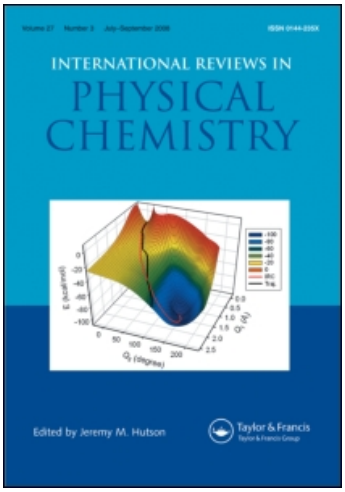

International Reviews in Physical Chemistry
Publication details, including instructions for authors and subscription information:
http://www.informaworld.com/smpp/title~content=t713724383

Coupled-channel calculations of excited-atom collisions

A. P. Hickman

Online publication date: 26 November 2010

To cite this Article Hickman, A. P.(1997) 'Coupled-channel calculations of excited-atom collisions', International Reviews in Physical Chemistry, 16: 2, 177 — 199
To link to this Article: DOI: 10.1080/014423597230262
URL: http://dx.doi.org/10.1080/014423597230262

INTERNATIONAL REVIEWS IN PHYSICAL CHEMISTRY, 1997, VOL. 16, NO. 2, 177–199

Coupled-channel calculations of excited-atom collisions

by A. P. HICKMAN

Department of Physics, Lehigh University, Bethlehem, PA 18015, USA

Recent calculations of excited-atom collisions based on the coupled-channel formalism are reviewed. Such calculations of electronic excitation processes require additional information (such as radial coupling matrix elements) beyond the adiabatic potential surfaces normally provided by *ab-initio* electronic structure calculations. Several examples are discussed that illustrate various strategies for obtaining this additional information. The first example involves collisions of heavy atoms, particularly xenon. In this case, the inner-shell electrons exhibit relativistic effects, and the effects of the spin–orbit operator can be quite large. In addition, the open-shell core has non-zero spin and orbital angular momentum. For these collisions the inner-shell electrons are treated using effective core potentials, and a model Hamiltonian is developed to handle the large spin–orbit effects and the open-shell core. The second example involves collisions in which the target atoms are spatially aligned. These calculations required radial coupling terms as well as the determination of explicit state-to-state cross-sections between specific angular momentum states. These examples demonstrate that collisions of a high level of complexity can now be quantitatively treated.

1. Introduction

For many years the coupled-channel (or close-coupling) method has been the standard for the most accurate and reliable scattering calculations. Because the method is based on a direct solution of Schrödinger's equation, the accuracy of the results achieved is limited only by the accuracy with which one can determine the potential surfaces and coupling terms for the particles involved in the collision. The method can been applied to electron–atom, electron–molecule, atom–atom, atom–molecule and molecule–molecule collisions. As the power of quantum chemistry computer codes has advanced, it has become possible to calculate *ab-initio* electronic potential surfaces and coupling matrix elements of greater reliability and for larger and more realistic systems.

There is an important contrast between rotational or vibrational excitation and electronic excitation processes. In the former case, the adiabatic *ab-initio* potential surface provides sufficient information for a coupled-channel dynamics calculation (unless, of course, excited electronic states play a role). In contrast, if electronic excitation is important, it is necessary to have potential surfaces for all important electronic states, as well as the coupling terms between these surfaces. These coupling terms, which are usually referred to as radial and angular coupling, are difficult to calculate.

This article reviews a selection of the present author's recent work that illustrates several strategies for obtaining the additional information that is necessary to treat electronic excitation processes. Two main areas have been addressed. First, scattering calculations have been extended to the realm of heavy atoms, particularly xenon. In this case, there are so many electrons that the inner shells exhibit relativistic effects, and the effects of the spin–orbit operator can be quite large. Another complication in this case is that the excited xenon atom has a structured core. That is, the core has

0144–235X/97 $12·00

orbital and spin angular momentum. This situation is more difficult to handle than, for example, the case of an excited alkali atom, which consists of a single electron in an excited orbital outside a closed-shell core. Second, calculations have been performed that provide detailed information about collisions in which the initial atoms are spatially aligned. These calculations require a high level of accuracy of the underlying *ab-initio* molecular potential curves, but they offer the opportunity to compare with the most recent and precise experimental data.

Section 2 provides a brief sketch of the coupled-channel method. It is intended to indicate how the quantities provided in electronic structure calculations are incorporated in a dynamics calculation. Section 3 discusses recent work on collisions of excited Xe atoms with rare gases He and Ar. These collisions have an important effect on the populations of various excited states of Xe in the atomic xenon laser. Section 4 summarizes recent calculations on the collisions of aligned Ca atoms with He. This work was stimulated by the recent experiments of Leone's group at the University of Colorado. By careful control of the polarizations of the exciting lasers, these experiments permit the excitation of spatially aligned excited states. Section 5 contains concluding remarks.

2. Outline of coupled-channel method

2.1. *Form of the coupled equations*

This section presents a brief sketch of the coupled-channel method. Many details will be omitted since they can be determined from extensive material already in the literature (Lester and Bernstein 1968, Gordon 1969, Smith 1969, Thorson 1969, McQuire and Kouri 1974, Pack 1974, Secrest 1975, Delos 1981). The intention is to illustrate the structure of the scattering equations that must be solved and how the various interatomic potential energy curves and coupling matrix elements are related to what is normally available from an *ab-initio* electronic structure calculation. We shall discuss a system that can be described by a Hamiltonian

$$H = -\frac{\hbar^2}{2\mu}\nabla_R^2 + H_0(R, \mathbf{r}). \tag{1}$$

The first term describes the relative motion of the projectile and the target, and the second term is the Hamiltonian of the collision partners, with R taken to be a fixed parameter. R is the relative coordinate of the two atoms, and we let $\mathbf{r}$ collectively denote all the internal coordinates of the two atoms. In many cases, $H_0(R, \mathbf{r})$ is what is called the electronic Hamiltonian, but for the present discussion we shall reserve that term since we shall deal with systems in which H_0 also has a spin–orbit term.

The task is to solve Schrödinger's equation for a fixed positive value of the energy E:

$$(H - E)\,\psi(R, \mathbf{r}) = 0. \tag{2}$$

The following expansion for ψ is assumed:

$$\psi(R, \mathbf{r}) = \sum_n F_n(R)\,\chi_n(R, \mathbf{r}). \tag{3}$$

At this point, the expansion functions $\chi_n(R, \mathbf{r})$ are not specified in detail. They are only required to satisfy

$$\int \chi_m(R, \mathbf{r})\,\chi_n(R, \mathbf{r})\,\mathrm{d}^3\mathrm{r} = \delta_{mn}. \tag{4}$$

We now substitute the assumed form for $\psi(R, \mathbf{r})$ (equation (3)) into equation (2). The standard procedure is to multiply by $\chi_m(R, \mathbf{r})$ and integrate over $\mathbf{r}$ to obtain a set of coupled equations for the functions $F_n(R)$. This procedure has a number of subtleties, primarily because the expansion functions $\chi_m(R, \mathbf{r})$ are normally expressed in the molecular frame. That is, the electronic coordinates $\mathbf{r}$ are most naturally expressed in coordinates relative to the internuclear axis, and this axis rotates during the course of the collision. This subject has been considered at length in the literature. The result (Smith 1969) is that the set of coupled equations for $F_n(R)$ has the following form:

$$\left(\mathbf{1}\frac{\mathrm{d}^2}{\mathrm{d}R^2} + \mathbf{A}(R)\frac{\mathrm{d}}{\mathrm{d}R} + \mathbf{U}(R)\right)\mathbf{F}(R) = 0, \tag{5}$$

where the elements of the matrix $\mathbf{A}(R)$ are determined (Smith 1969) from the terms

$$P(R)_{mn} = \int \chi_m(R, \mathbf{r})\frac{\mathrm{d}}{\mathrm{d}R}\chi_n(R, \mathbf{r})\,\mathrm{d}^3r. \tag{6}$$

These matrix elements constitute the radial coupling. They are a measure of how rapidly the electronic configurations of the wavefunctions $\chi_m(R, \mathbf{r})$ change with R. If the $P(R)_{mn}$ are small enough to be neglected then $\mathbf{A}(R) = 0$, and the first derivative term in equation (5) vanishes. The other terms in equation (5) are defined by

$$U(R)_{mn} = \frac{2\mu}{\hbar^2}[(E - E_n)\,\delta_{mn} - V(R)_{mn} - V_c(R)_{mn}], \tag{7}$$

$$V(R)_{mn} = \int \chi_m(R, \mathbf{r})\,H_0(R, \mathbf{r})\,\chi_n(R, \mathbf{r})\,\mathrm{d}^3r \tag{8}$$

and $V_c(R)_{mn}$ are the centrifugal potential terms, which depend on the details of the definition of the $\chi_m(R, \mathbf{r})$. In most of the present work, these terms can be derived analytically (Walker and Light 1975).

The solution to equation (5) is represented as a matrix $\mathbf{F}(r)$. The elements of each column correspond to the $F_n(R)$ in equation (3), and there are N linearly independent solutions. The scattering matrix elements and cross-sections are determined from the asymptotic form of the solution matrix.

2.2. *Selection of expansion functions* $\chi_n(R, \mathbf{r})$

Several choices can be made for the expansion functions $\chi_n(R, \mathbf{r})$, and the choice influences the form (5) of the coupled equations. In general, one can make specific types of choices for $\chi_n(R, \mathbf{r})$ that will make certain terms in equation (5) vanish. The most straightforward choice is to let the $\chi_n(R, \mathbf{r})$ be the eigenfunctions of the internal Hamiltonian H_0. That is

$$H_0\,\chi_n(R, \mathbf{r}) = E_n(R)\,\chi_n(R, \mathbf{r}). \tag{9}$$

For this choice the electronic coupling matrix V_{mn} becomes diagonal: $V_{mn} = E_n(R)\delta_{mn}$. If H_0 is taken to be the electronic Hamiltonian for the scattering system, then the $E_n(R)$ are just the adiabatic potential curves (as functions of R), and the $\chi_n(R, \mathbf{r})$ are the corresponding electronic wavefunctions at each R. The $\chi_n(R, \mathbf{r})$ would be the electronic wavefunctions normally calculated by *ab-initio* electronic structure techniques. Note that these calculations are normally performed for several different values of the parameter R.

This choice leads to the so-called adiabatic representation. At every R, the potential curves are taken to have their adiabatic values, and the 'potential coupling terms', that is, the off-diagonal elements of V_{mn}, are always zero. The dynamical coupling that causes transitions between states comes from the radial coupling terms $P(R)_{mn}$ (which determine $\mathbf{A}(R)$) and from rotational coupling terms, which would be included in the $V_c(R)_{mn}$. An issue with the adiabatic representation is that the matrix elements $P(R)_{mn}$ are not routinely determined by electronic structure codes.

A second choice of the expansion functions is to select, by some criteria, $\chi_n(R, \mathbf{r})$ that are in some sense 'smooth' and have such a small dependence on R that the $P(R)_{mn}$ terms can be neglected. This choice leads to the diabatic representation. The advantage here is that the radial coupling terms, which may be difficult to evaluate, are not needed, and the differential equation (5) is simpler in form because the first-derivative terms do not appear. The terms that induce the transitions arise because the 'smooth' $\chi_n(R, \mathbf{r})$ are not usually eigenfunctions of H_0. In this case the potential coupling matrix $V(R)_{mn}$ has off-diagonal terms, which couple different electronic states.

In a wide class of collision problems, there is a third choice for the expansion coefficients that offers advantages of both choices previously mentioned. One can use directly the results of *ab-initio* calculations, but no $\mathrm{d}/\mathrm{d}R$ matrix elements are explicitly required. In collisions in which transitions among fine-structure levels are important, it is often possible to write

$$H_0 = H_{\mathrm{elec}}(R) + H_{\mathrm{so}}. \tag{10}$$

Here the internal Hamiltonian of the projectile–target system has been partitioned into the standard electronic component, which depends explicitly on the internuclear separation, plus a spin–orbit term. For many important systems, it is justified to assume that H_{so} is independent of R. In this case, we can begin with the adiabatic potential curves for $H_{\mathrm{elec}}(R)$ calculated using the full machinery of quantum chemistry and then, with modest additional effort, include the effects of the spin–orbit operator. This method was originally developed by Cohen and Schneider (1974) and applied to Ne_2^* and Ne_2^+. With some modifications, we have applied similar techniques to treat collisions of Xe* with He and Ar (Hickman *et al.* 1992, 1993), and collisions of $O(^3P_J)$ with O^+ (Hickman *et al.* 1997). We have also applied a similar method to fine-structure-changing collisions of $K(4\,^2P)$ and $Rb(5\,^2P)$ with diatomic molecules (Hickman 1981, 1982).

The key point is that the basis functions that describe the angular momentum states of $H_{\mathrm{elec}}(R)$ and those that describe the corresponding states of H_{so} are related by a unitary transformation that can be expressed in terms of Clebsch–Gordan coefficients (Cohen and Schneider 1974). For example, the states of $H_{\mathrm{elec}}(R)$ are usually expressed in an LS coupling scheme, and those of H_{so} in jj coupling. A standard example is an alkali atom $A(^2P_J)$ and a rare gas $X(^1S_0)$. Then the electronic and spin angular momenta of AX are $L = 1$ and $S = 1/2$, which can couple to give $j = 1/2$ or $j = 3/2$. The eigenfunctions of $H_{\mathrm{elec}}(R)$ are best expressed in LS coupling. They are written $|LM_L SM_S\rangle$ and satisfy

$$\langle LM'_L SM'_S | H_{\mathrm{elec}}(R) | LM_L SM_S \rangle = \delta_{M'_L M_L} \delta_{M'_S M_S} V_\Lambda(R), \tag{11}$$

where we use the notation $\Lambda|M_L|$, and $\Lambda = 0$ corresponds to a Σ state and $\Lambda = 1$ to a Π state. In other words, one can use standard *ab-initio* codes to determine Σ and Π potential curves $V_\Sigma(R)$ and $V_\Pi(R)$. The next step is to use the unitary transformation

between LS and jj coupling to construct the eigenfunctions of H_{so}. These eigenfunctions are denoted $|LSjm\rangle$ and satisfy

$$|LSjm\rangle = \sum_{M_L}\sum_{M_S} \langle LM_L SM_S|jm\rangle |LM_L SM_S\rangle, \tag{12}$$

$$H_{so}|LSjm\rangle = E_j|LSjm\rangle, \tag{13}$$

where $\langle LM_L SM_S|jm\rangle$ is a Clebsch–Gordan coefficient and the energies of the spin–orbit levels E_j are normally available from spectroscopy. We now choose the functions $\chi_n(R, \mathbf{r})$ to be the $|LSjm\rangle$. Using equations (11)–(13), and noting that jm is the state label, the potential coupling matrix elements can then be shown to be

$$V_{j'm',jm}(R) = \sum_{M_L}\sum_{M_S} \langle LM_L SM_S|j'm'\rangle \langle LM_L SM_S|jm\rangle V_\Lambda(R). \tag{14}$$

Normally, the radial coupling terms in the LS representation are negligible, and the transformation between LS and jj coupling is independent of R. Then the matrix $\mathbf{A}(R)$ in equation (5) is zero and the first-derivative terms vanish.

This example shows that one can formulate the coupled-channel problem for fine-structure collisions in a way that incorporates the adiabatic LS potential curves determined by *ab-initio* calculations. The scattering equation (5) has no first-derivative terms, because all the state-to-state coupling terms arise from the off-diagonal terms in equation (14).

3. Collisions of Xe* with He and Ar

3.1. *Introduction: role of collisions in the atomic xenon laser*

This section reviews our recent investigation of collisions of excited Xe with He and Ar (Hickman *et al.* 1992, 1993). Such collisions play a crucial role in the kinetics of the atomic Xe laser. This laser operates on several infrared transitions from 5d to 6p levels of excited Xe. The laser transitions are indicated on the energy level diagram in figure 1. Although the details of the kinetics are not fully understood (Alford and Hays 1989, Ohwa *et al.* 1989), the general scheme may be sketched as follows. The laser gas mixture typically consists of a few per-cent Xe in a buffer of He and Ar. Xe is ionized by electron-beam pumping, or in some cases by nuclear pumping (Alford and Hays 1989):

$$\mathrm{Xe} \rightarrow \mathrm{Xe}^+ + \mathrm{e}. \tag{15}$$

Various three-body association reactions are thought to lead to the formation of ArXe^+:

$$\mathrm{Xe}^+ + 2\mathrm{Ar} \rightarrow \mathrm{ArXe}^+ + \mathrm{Ar}. \tag{16}$$

Various excited states of Xe can then be produced by dissociative recombination:

$$\mathrm{ArXe}^+ + \mathrm{e} \rightarrow \mathrm{Xe}^{**} + \mathrm{Ar}. \tag{17}$$

The distribution of excited states Xe** is not known. It is possible that some of the 5d upper levels are produced directly by dissociative recombination, but probably more likely that additional collisional and radiative processes convert more highly excited Xe** to 5d levels. Xe_2^+ may also be produced in the laser. It is thought (Ohwa *et al.* 1989) that dissociative recombination of Xe_2^+ directly produces the lower laser levels Xe*(6p). This process, which would degrade the population inversion, is suppressed in practice by avoiding large concentrations of Xe.

Collisions of Xe** with buffer gas atoms are important because these collisions strongly influence the populations of the upper and lower laser levels. Experimental studies originally observed a tremendous variation in specific state-to-state transition rates. Because of this variation, adjusting the concentrations of He and Ar in the buffer

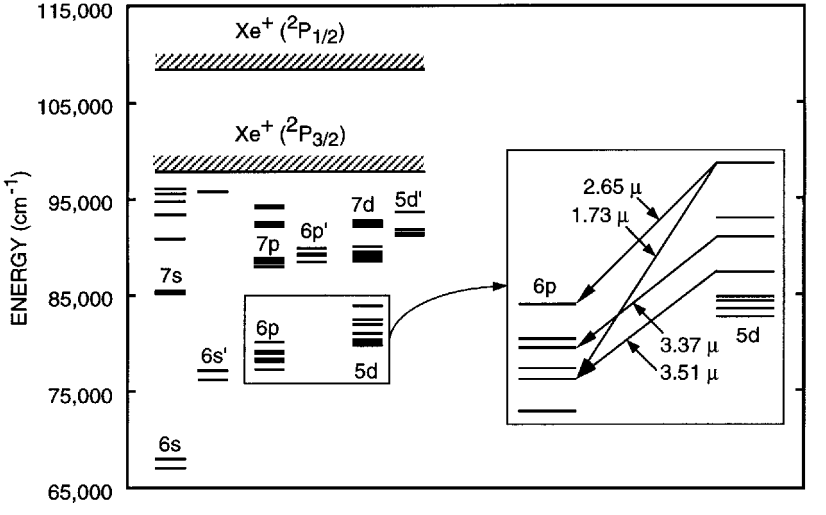

Figure 1. Energy level diagram for atomic Xe. Energies are given relative to the ground state Xe($5p^6$). Both Xe^+ fine-structure levels are shown. The inset shows selected $5d \rightarrow 6p$ transitions for the atomic Xe laser.

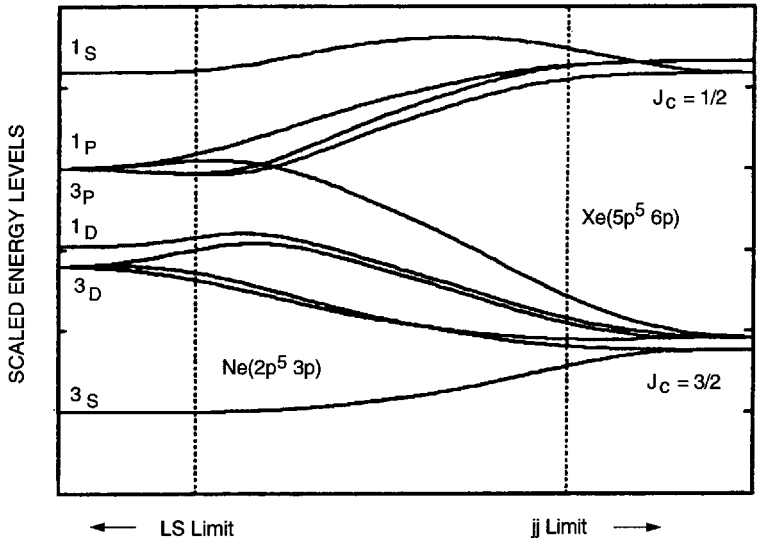

Figure 2. The transition between *LS* and *jj* coupling shown in the style of Condon and Shortley (1967). Scaled energy levels are presented as a function of a parameter related to the relative strength of the spin–orbit and electrostatic terms in the atomic Hamiltonian. The dotted lines correspond approximately to the coupling that exists in Ne and Xe.

gas lead to the selective quenching of the lower level of one or the other of the laser transitions. The population inversion and hence the gain on specific transitions can thereby be controlled. To exploit this situation, a detailed understanding of the state-to-state collision processes was needed. However, the early studies found no simple correlation with the degree of inelasticity or the mass or polarizability of the collision partner. This situation suggested that a convincing theoretical analysis would require high-quality excited-state potential curves and matrix elements, and a detailed treatment of the dynamics.

3.2. *Potential curves and matrix elements*

Electronic structure calculations to determine excited-state potential curves for systems such as XeHe and XeAr present special problems because of the large number of inner-shell electrons, which exhibit relativistic effects, and the large spin–orbit interactions. Theoretical treatment of the dynamics is also a challenging problem. A significant physical feature is the structured core of the Xe atom. The $Xe^+(5p^5)$ core has spin and orbital angular momenta that can participate in the collision. This complexity is absent in the more frequently studied case of collision of excited alkali atoms with rare gases, because the core of the alkali atom is a closed shell.

Applying the standard procedures discussed in section 2 to calculate potential curves and matrix element, and then using the results in a coupled-channel calculation, was not feasible for XeHe or XeAr. Calculating the adiabatic eigenfunctions $\chi_n(R, \mathbf{r})$ for the Hamiltonian H_0, including both inner-shell effects and the spin–orbit operator, is tractable using the effective core potentials developed by Pitzer and co-workers (Pitzer and Winter 1988, Chang and Pitzer 1989), but this method had not been extended to provide the radial coupling matrix elements. Another option would have been to include the inner shell effects in the calculation of the eigenfunctions $\chi_n(R, \mathbf{r})$ of the appropriate electronic Hamiltonian $H_{\text{elec}}(R)$, and then to add the spin–orbit effects afterwards by a subsequent diagonalization of $H_{\text{elec}}(R) + H_{\text{so}}$. In this case, the extremely large size of the spin–orbit matrix elements for Xe led to concern that this method would not be sufficiently accurate. The approach that we adopted was to develop an analytic model that enabled us to combine the information determined from *ab-initio* electronic structure calculations with available spectroscopic information. The method allowed us to determine realistic potentials and coupling matrix elements.

The importance of spin–orbit effects in Xe can be illustrated by comparison with the corresponding effects in lighter atoms. For example, the method of treating $H_{\text{elec}}(R) + H_{\text{so}}$ was originally applied to Ne_2^*. In this case the electronically excited states of the molecule are affected by the spin–orbit splitting of the Ne^+ core states $2p^5$ ^2P_J, for $J = 1/2$ and $3/2$. This splitting is 782 cm^{-1}. For excited states of XeHe and XeAr, the corresponding quantity is the 10 537 cm^{-1} splitting of the Xe^+ core states $5p^5$ ^2P_J. For the Ne systems, the spin–orbit operator is a small effect that leads to some perturbation of the *LS* states. For the Xe systems, the reorganization of the levels is much stronger. We can consider the energy spectrum of an artificial atomic Hamiltonian H' to illustrate quantitatively how these two systems differ. Consider

$$H' = (2-q)\,H_{\text{elec}} + qH_{\text{so}}. \tag{18}$$

For $0 \leqslant q \leqslant 2$, we can calculate the eigenvalues of H'. The case $q = 0$ corresponds to pure *LS* coupling and $q = 2$ corresponds to *jj* coupling. Figure 2 exhibits the relative energy level spectrum obtained numerically for various values of the parameter q. (The abscissa is a nonlinear function of q.) The dotted lines correspond approximately to the case of Ne, which is not far from *LS* coupling. The case $q = 1$, the physical $Xe(5p^5\,6p)$ atom, corresponds to an intermediate angular-momentum coupling scheme. This coupling scheme can be well described analytically by so-called pair coupling (Saraph and Seaton 1977)

$$L_c + S_c = J_c, \quad J_c + l = K, \quad K + s = J, \tag{19}$$

where L_c, S_c and J_c refer to the orbital, spin and total angular momentum of the np^5 ^2P_J ion, s is the spin of the valence electron and J is the total angular momentum of the

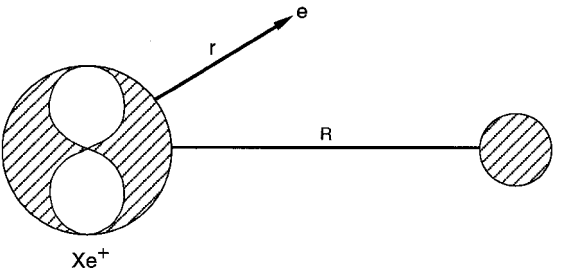

Figure 3. Schematic illustration of the model used to formulate the interaction of an excited Xe atom with a rare gas. The Xe^+ core has an unfilled 5p electron orbital.

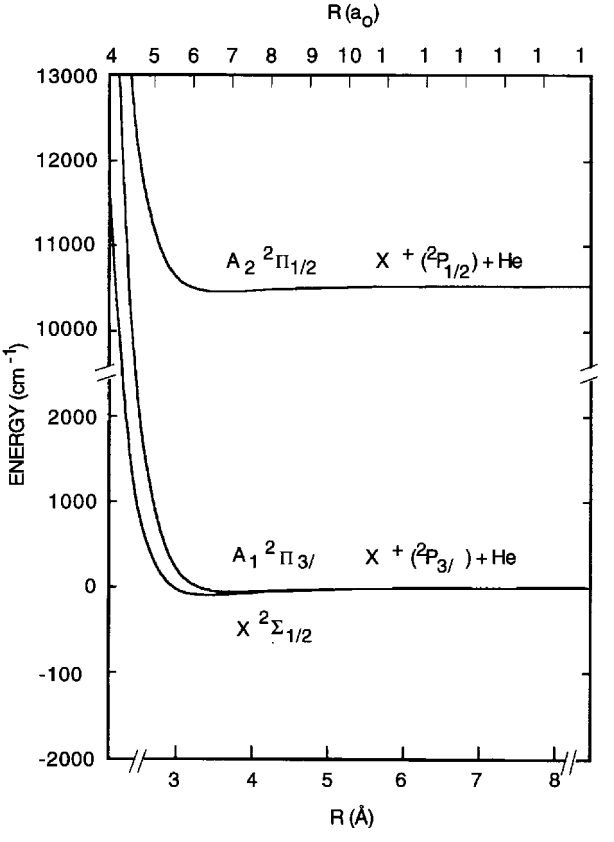

Figure 4. $HeXe^+$ potentials.

atom. These quantum numbers are used in the conventional state labels $nl[K]J$. (Moore 1958). However, this analytic coupling scheme does not provide an adequate description of the 6s and 5d levels. In particular, there is strong mixing of the 6s′ and lower 5d levels. For these levels, the numerically determined atomic eigenfunctions exhibit a mixture of $J_c = 3/2$ and $J_c = 1/2$ basis functions.

The details of the calculations of the potential curves have appeared elsewhere (Hickman *et al.* 1992). Here only the key points will be summarized. The first step is to perform *ab-initio* electronic structure calculations for Xe*Ar. These calculations used the method developed by Pitzer and co-workers (Pitzer and Winter 1988, Chang and Pitzer 1989). The effect of the inner-shell electrons on each orbital outside the core is

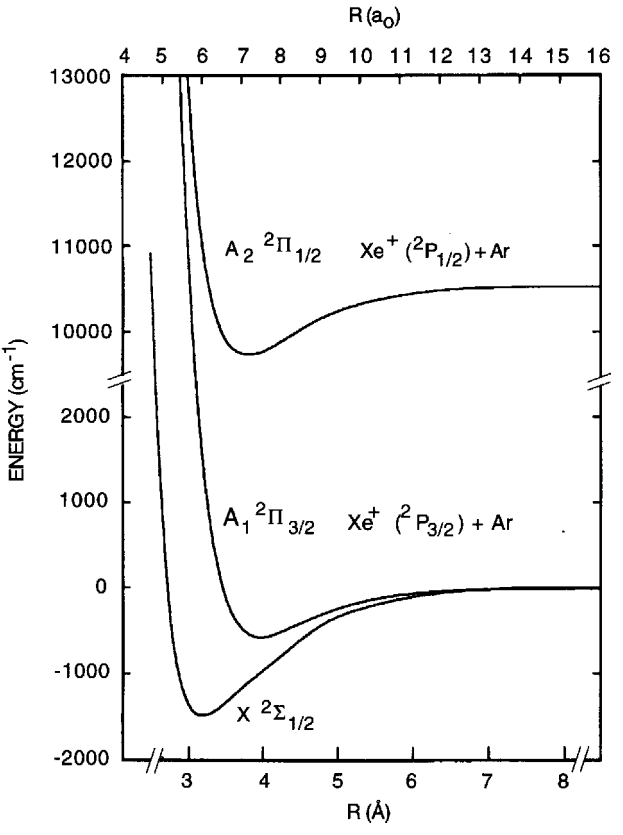

Figure 5. $ArXe^+$ potentials.

represented by a relativistic effective potential (REP). The REP for each orbital depends on the angular momentum numbers l and j and is determined from a numerical solution of the relativistic Dirac–Fock equation. Then the REPs for two orbitals having $j = l + 1/2$ and $j = l - 1/2$ are replaced by their weighted average and difference. The averaged REP depends only on l and can be easily implemented with standard electronic codes. The difference between the REPs provides an approximate description of the true spin–orbit interaction. The spin–orbit operator is incorporated in the calculation at the configuration interaction (CI) level. The final result is that Xe*Ar can be treated as a 16-electron problem.

Further refinement of the *ab-initio* calculations was necessary before proceeding with the scattering calculations. Because the energy levels of Xe (including fine structure) are so closely spaced ($\Delta E \approx 100$–1500 cm^{-1}), particular attention was paid to the accuracy of the asymptotic limits of the calculated potential curves. Although accurate by conventional standards, the *ab-initio* calculations did not provide asymptotes of the exceptional precision needed for the scattering calculations. In addition, the *ab-initio* calculations provided only the adiabatic potential curves, that is, the eigenvalues of the total Hamiltonian H_0 at each internuclear distance R. Also necessary for a scattering calculation are the matrix elements coupling the various potential curves. To insure accurate asymptotes, and to obtain the necessary coupling matrix elements, we developed a method to refine and extend the *ab-initio* calculations.

The method was based on defining a model Hamiltonian. As illustrated in figure 3,

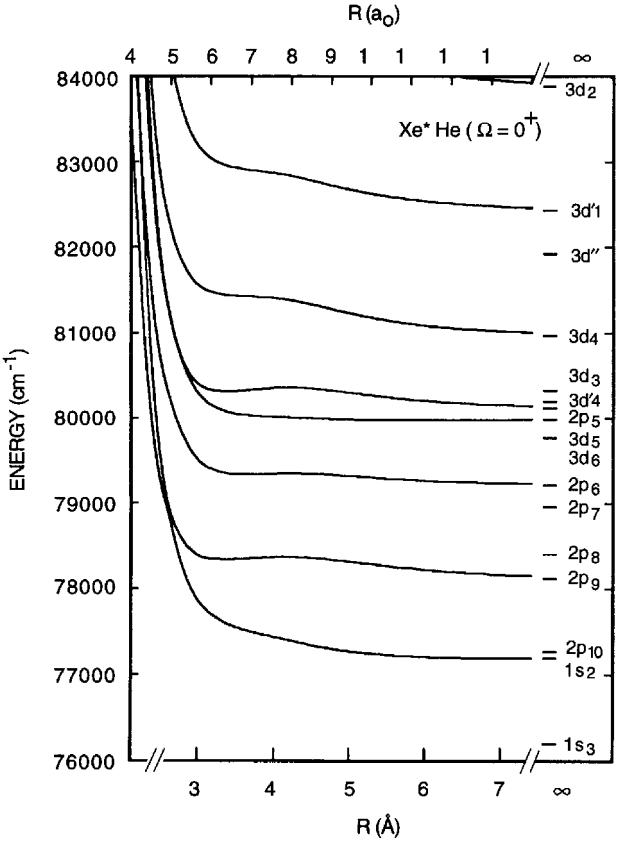

Figure 6. Xe*He potentials for $\Omega = 0^+$.

the physical scattering system is composed of an incident rare-gas atom and an excited Xe atom, which consists of an excited electron and an ion core. H_0 was partitioned into three terms that described the interactions between each pair of components of the full system. The essential physical approximations in our method are the same as those used successfully to describe fine-structure-changing collisions of excited ^{2}P alkali atoms with rare gases (Reid 1973, Nikitin 1975). The only difference in the present case is that the spin and orbital angular momentum of the ion core are non-zero and must be included in the electronic wavefunction. This extra feature can be fully incorporated by treating the atomic portion of the model Hamiltonian (Xe^+–Rg) as a two-electron system, that is one valence electron and one core hole. The details of this method have been presented by Condon and Shortley (1967). The result is that our model Hamiltonian is based on the same physics used to treat simpler fine-structure-changing collisions; only the algebra is more complicated.

The model Hamiltonian depends on a small set of physically sensible parameters. Our strategy is to determine the parameters of the model Hamiltonian that fit the *ab-initio* potentials and then selectively to modify certain parameters that can be more accurately determined from spectroscopy or other experimental data. The model Hamiltonian is fully determined by the final set of parameters, and it is possible to determine both the adiabatic potential curves and the coupling matrix elements needed for the scattering calculations.

Selected results are shown in figures 4–9. Figures 4 and 5 show adiabatic potential

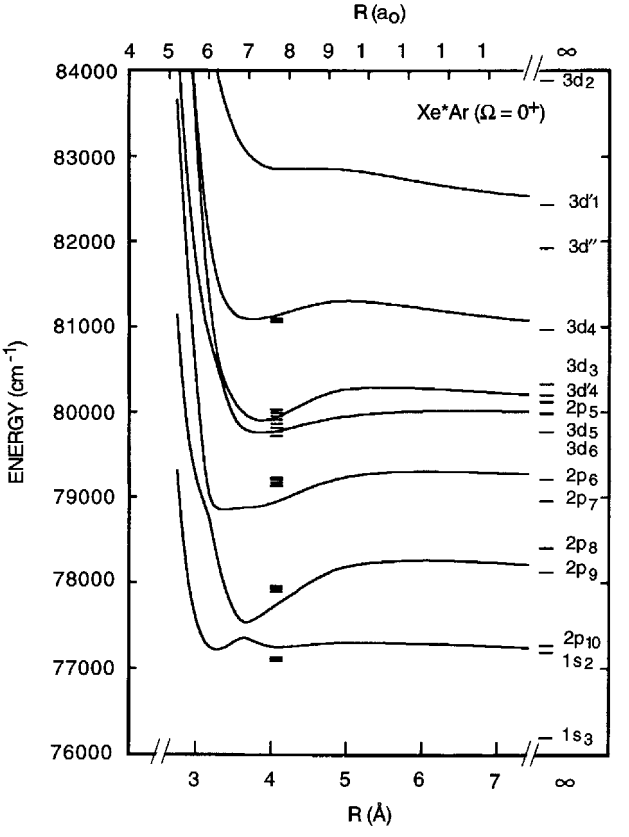

Figure 7. ArXe* potentials for $\Omega = O^+$. The marks near 4 Å correspond to observed vibrational levels.

curves determined by Hickman *et al.* (1992) for $HeXe^+$ and $ArXe^+$ respectively. Many of the differences in the potentials for excited states of Xe*He and Xe*Ar can be traced to differences in the well depths of the underlying ionic curves. Figures 6 and 7 show the potentials for $\Omega = 0^+$, and figure 8 and 9 show the potentials for $\Omega = 0^-$. These particular curves have been selected because they illustrate several interesting results of the scattering dynamics, which will be discussed in the next section.

3.3. *Results of coupled-channel calculations*

Coupled-channel calculations have been performed for Xe* collisions with He and Ar. Inelastic cross-sections were calculated for all transitions among the 6s′, 6p and 5d levels of Xe. (According to the usual notation, an unprimed level refers to a state whose ion core is the ground state $Xe^+(5p^5\ ^2P_{3/2})$, and a primed level has the excited core $Xe^+(5p^5\ ^2P_{1/2})$.) The levels included in the calculation are included in the table. The calculations for the + and − symmetries each included 34 channels.

Calculations were performed for total energies spaced approximately at intervals of 200 cm^{-1} from 77400 to 84000 cm^{-1}, where all energies are relative to the $Xe(5p^6)$ ground state. We determined cross-sections for transitions among the 6s′, 6p and 5d levels. The results for those transitions found to be most important are shown in figures 10 and 11. These figures present our most detailed results. We also used these

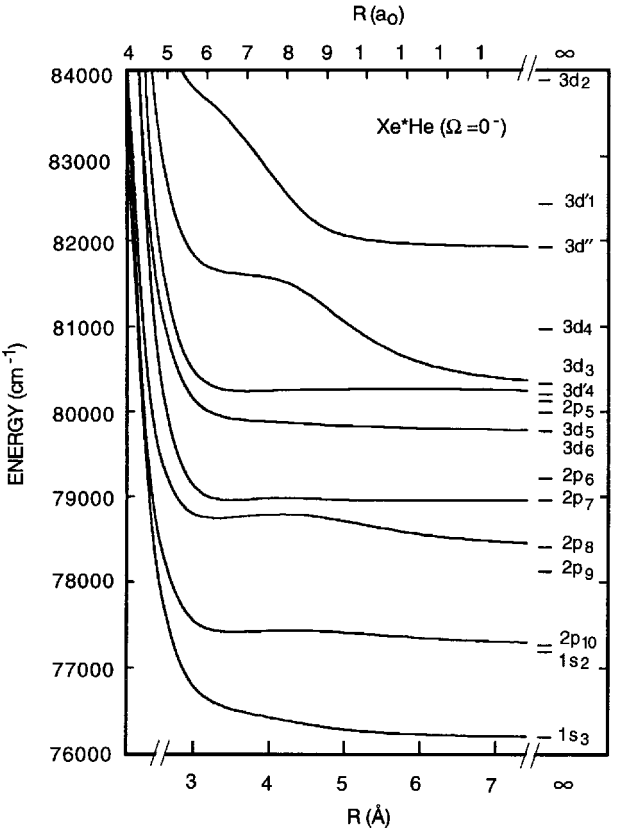

Figure 8. Xe*He potentials for $\Omega = 0^-$.

cross-sections to obtain the transition rates at $T = 300$ for all the level-to-level transitions. The rates may be expressed as the thermal average of the velocity times the cross-section:

$$k_{\beta\to\beta'}(T) = \langle v\sigma_{\beta\to\beta'}\rangle. \tag{20}$$

The index β refers to the levels listed in the table. This formula can be conveniently expressed as

$$k_{\beta\to\beta'}(T) = \bar{v}\int_0^\infty \sigma_{\beta\to\beta'} E \exp\left(-\frac{E}{kT}\right)(kT)^{-2}\,\mathrm{d}E, \tag{21}$$

where $\bar{v}$ is the average thermal velocity:

$$\bar{v} = \left(\frac{8kT}{\pi\mu}\right)^{1/2}. \tag{22}$$

The broken curves in figures 10 and 11 are proportional to the Maxwellian energy distribution $E\exp(-E/kT)$ at $T = 300$ K and give an indication of the energy range of the cross-section that contributes to the rate constants. The original work also presented rate constants at $T = 800$ K.

One of the major results of the investigation was the extreme variation in the transition rate constants, depending on the specific states involved and the collision

Levels included in the calculations.

No.	Paschen	*Jl* coupling	Energy† (cm^{-1})
1	$1s_3$	$6s'[1/2]_0$	76197·292
2	$1s_2$	$6s'[1/2]_1$	77185·560
3	$2p_{10}$	$6p[1/2]_1$	77269·649
4	$2p_9$	$6p[5/2]_2$	78120·303
5	$2p_8$	$6p[5/2]_3$	78403·562
6	$2p_7$	$6p[3/2]_1$	78956·538
7	$2p_6$	$6p[3/2]_2$	79212·970
8	$3d_6$	$5d[1/2]_0$	79771·798
9	$3d_5$	$5d[1/2]_1$	79987·160
10	$2p_5$	$6p[1/2]_0$	80119·474
11	$3d'_4$	$5d[7/2]_4$	80197·160
12	$3d_3$	$5d[3/2]_2$	80323·280
13	$3d_4$	$5d[7/2]_3$	80970·930
14	$3d''$	$5d[5/2]_2$	81926·040
15	$3d'_1$	$5d[5/2]_3$	82430·720
16	$3d_2$	$5d[3/2]_1$	83890·470

† From Moore (1958); energies are relative to the Xe($5p^6$) ground state.

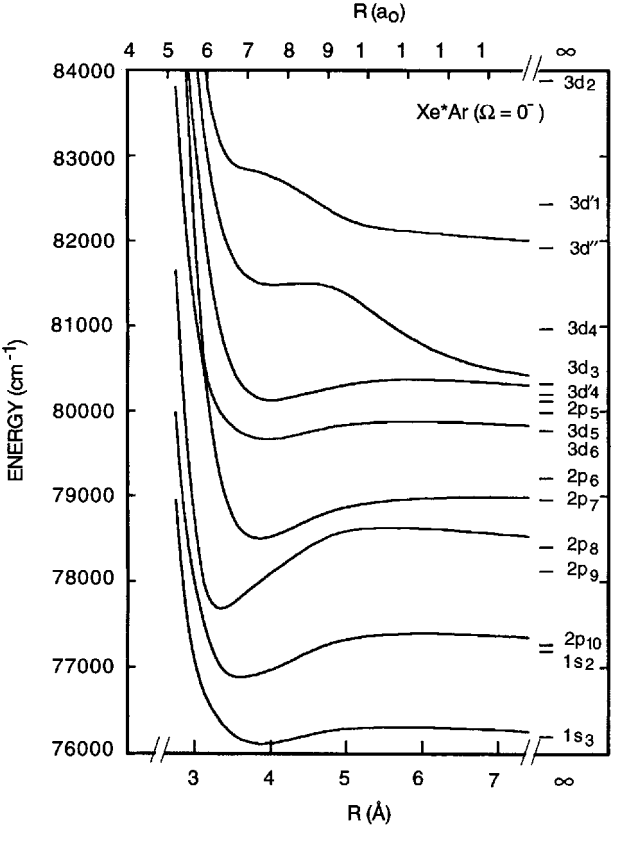

Figure 9. Xe*Ar potentials for $\Omega = 0^-$.

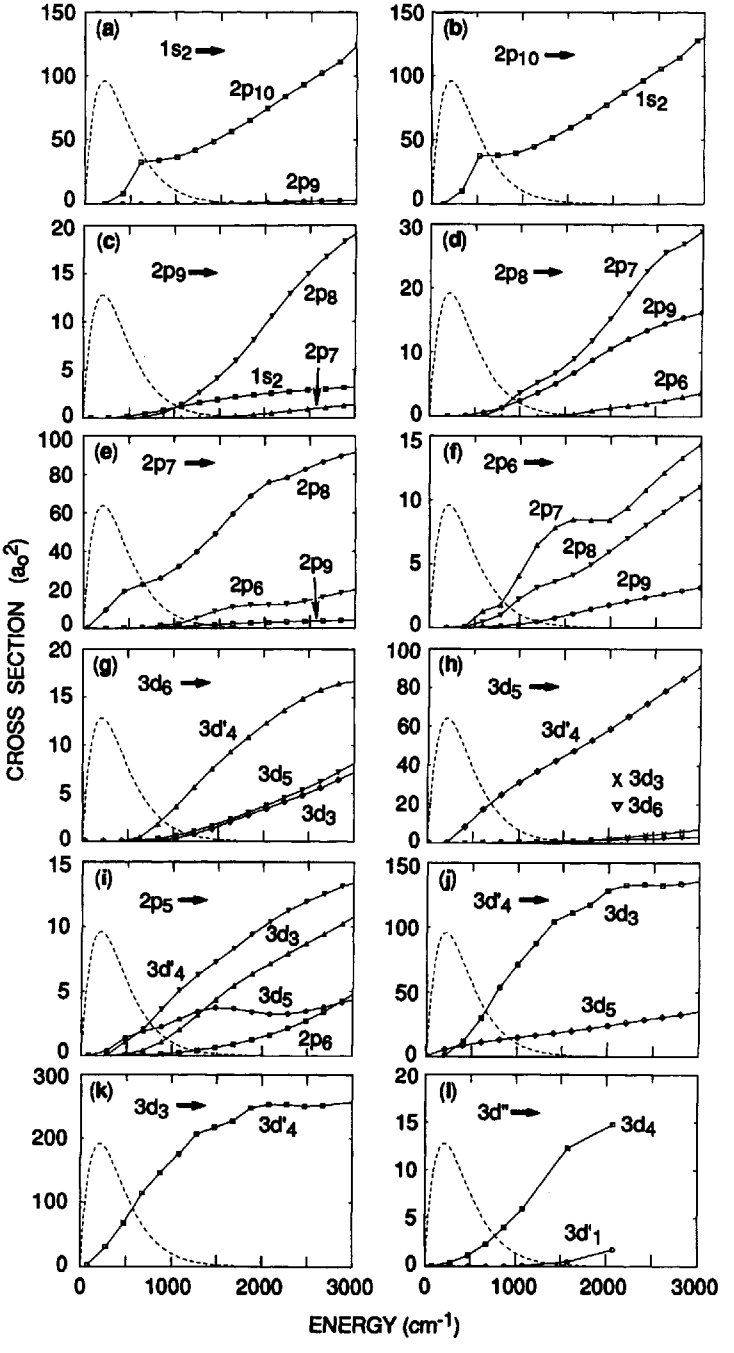

Figure 10. (*a*)–(*l*) Level-to-level cross-sections as a function of incident kinetic energy calculated for Xe*+He for various indicated initial states. The broken lines are the distributions of thermal energies used to calculate the rate constant at $T = 300$ K. Only the largest cross-sections are shown.

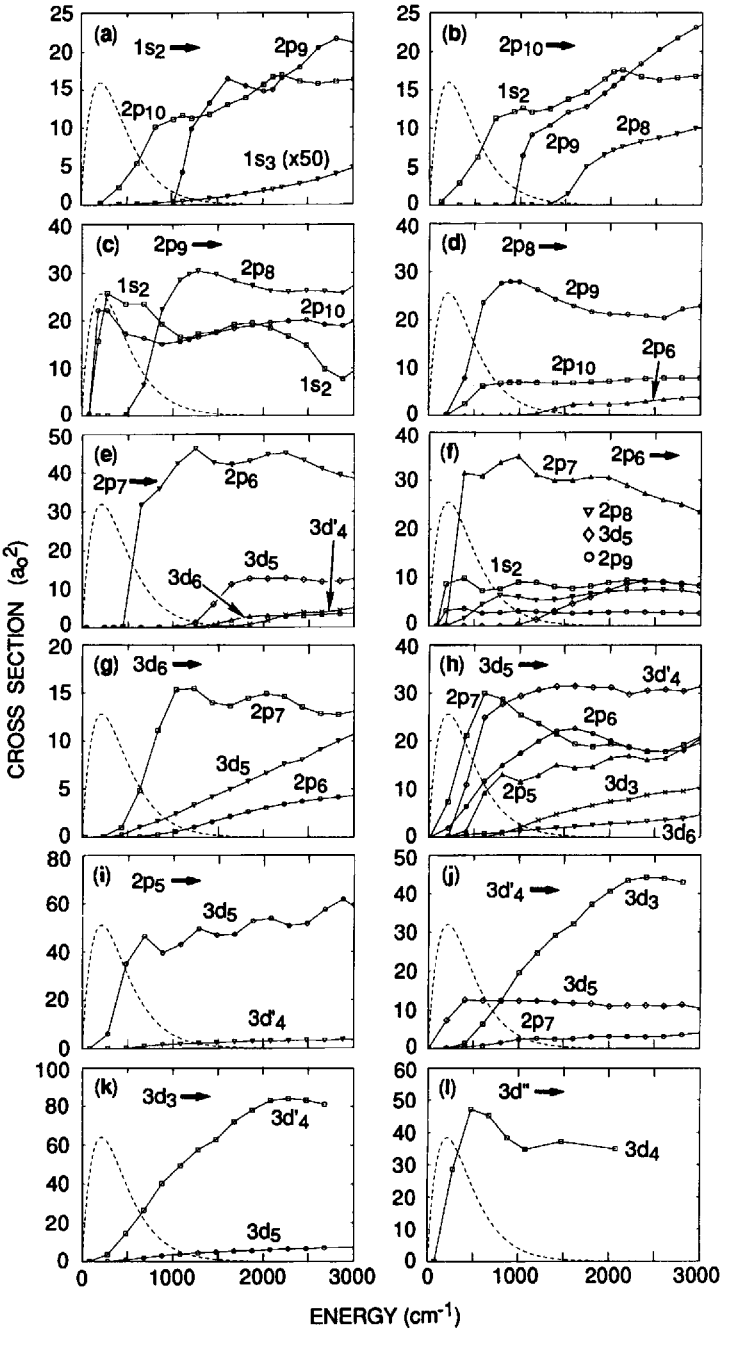

Figure 11. (*a*)–(*l*) Level-to-level cross-sections as a function of incident kinetic energy calculated for Xe* + Ar for various indicated initial states. The broken lines are the distributions of thermal energies used to calculate the rate constant at $T = 300$ K. Only the largest cross-sections are shown.

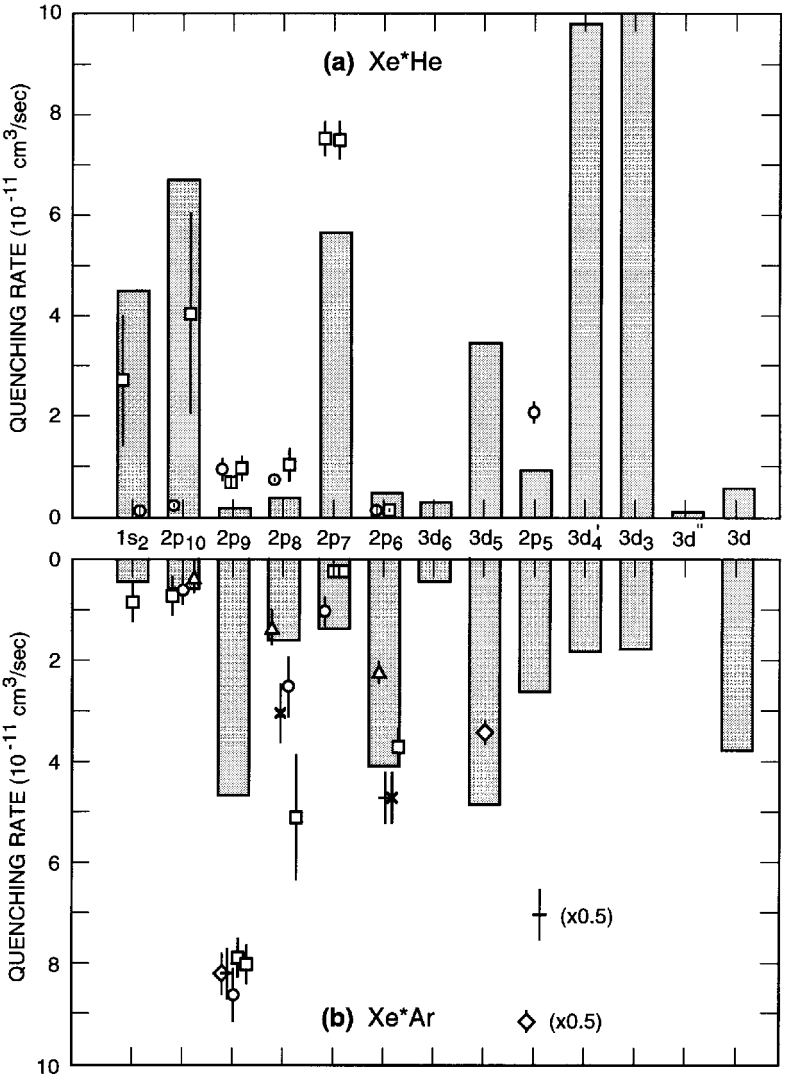

Figure 12. Total quenching rates of specific excited states of Xe (*a*) by He and (*b*) by Ar, where the shaded bars are the present calculations, and the symbols are various experiments: (□), Alford (1992); (○), Xu and Setser (1990); ◇, Bruce *et al.* (1990); (——), Xu and Setser (1990); (△), Inoue *et al.* (1984); (×), Horiguchi *et al.* (1981).

partner. This variation is illustrated in figure 12. Rates for T = 300 K are shown. For each level, we have summed the rates for transitions to every other level (both higher and lower in energy). The bars on the upper portion of the diagram correspond to the theoretical calculations for He, and those on the lower portion to Ar. Experimental points are shown in the same way. Total Ar quenching rates for the initial $1s_2$ state have not been measured, but the available level-to-level rates enable us to obtain a lower bound. Figure 12 clearly indicates that some levels are quenched much more effectively than others. There are also clearly many cases where a level is effectively quenched by He and not by Ar, or where the opposite is true. On the whole, the theoretical calculations exhibit quite good agreement with the available experimental data. This agreement supports the reliability of the potential curves. Careful analysis

of the scattering calculations based on these potentials provides insight into the physics of the collision dynamics.

Two examples will serve to illustrate how the variation in the transition rate constants are directly related to the behaviour of the potential curves. Consider the total quenching rates for the initial states $2p_7$ and $2p_6$ shown in Fig. 12. The $2p_7$ level is effectively quenched by He but not by Ar, and the $2p_6$ level exhibits the reverse dependence. The potential curves and dynamics calculations provide a clear explanation for this behaviour.

A fairly high rate ($2{\cdot}4 \times 10^{-11}$ cm^3 s^{-1} at T = 300 K) for the transition of Xe $2p_6(6p[3/2]_2)$ to $1s_2(6s'[1/2]_1)$ induced by Ar was originally measured by Alford (1992). Because of the large energy gap between these states, the mechanism was not obvious. The potential curves in figure 7 provide an explanation. A sequence of two curve crossings leads from the initial $2p_6$ state to an intermediate state, and then to the $1s_2$ state. The coupled-channel calculations yield a rate of 1×10^{-11} cm^3 s^{-1} at T = 300 K, which confirms the two-crossings mechanism. The same transition is very weak if He is the collision partner. The potential curves shown in figure 6 for XeHe confirm that the sequence of curve crossings is not available for this system. Ultimately, the strong difference in the two sets of potential curves can be traced back to the very different well depths for the ion cores $HeXe^+$ and $ArXe^+$, as shown in figures 4 and 5.

State-to-state rates for the transition $2p_7(6p[3/2]_1)$ to $2p_8(6p[5/2]_3)$ induced by He and by Ar exhibit the opposite behaviours. The He rate is high, $7{\cdot}2 \times 10^{-11}$ cm^3 s^{-1} (Alford 1992), and the Ar rate is much lower, $0{\cdot}03 \times 10^{-11}$ cm^3 s^{-1} (Alford 1992) or $1{\cdot}0 \times 10^{-11}$ cm^3 s^{-1} (Xu and Setser 1990). The scattering calculations yield a rate of $5{\cdot}5 \times 10^{-11}$ cm^3 s^{-1} for He and $0{\cdot}01 \times 10^{-11}$ cm^3 s^{-1} for Ar. The calculations indicate that the mechanism for this transition is the avoided crossing in the $\Omega = 0^-$ states near 4 Å shown in figure 8 for He and figure 9 for Ar. The splitting at the crossing is somewhat less for He. Our results indicate that the lighter, faster He tends to traverse the coupling region diabatically. Conversely, the heavier, slower Ar tends to follow the adiabatic curves. The higher thermal velocity of He therefore has a double effect; it accounts for a larger cross-section and also appears explicitly in the expression for the rate constant (the thermal average of velocity × cross-section).

We have reviewed detailed calculations of inelastic collisions of excited states of Xe with He and Ar. The potential curves and scattering calculations provide a framework for interpreting the extreme selectivity of the rates with respect to specific states and collision partners observed in several recent experimental studies. The dynamics are characterized by the interplay of different states of the excited atom's ionic core, and by intermultiplet as well as intramultiplet mixing (e.g. $6p \rightarrow 5d$ transitions). The calculations have provided an explanation for several puzzling experimental results, such as the $2p_6 \rightarrow 1s_2$ transition in Ar, which proceeds by a double curve crossing, and the difference between He and Ar for the $2p_7 \rightarrow 2p_8$ transition, which depends on subtle differences in the potential curves and the mass difference. In summary, the coupled-channel calculations have provided an explanation for a large amount of experimental data and demonstrate that collisions of this complexity can be quantitatively treated.

4. Collisions of aligned atoms: Ca(4s4f ^{1}F) + He

This section reviews our recent extension of the coupled-channel method to describe collisions of aligned atoms (Hickman *et al.* 1994). This work relies on *ab-initio* molecular potential curves for the He–Ca system, and on radial coupling matrix elements between these curves.

The extension of the coupled channel method has been driven by recent advances in experimental techniques. In a series of elegant experiments (Hale *et al.* 1984, Bussert *et al.* 1987, Robinson *et al.* 1990, Driessen *et al.* 1991a, b), Leone's group has investigated collision process involving excited Ca atoms prepared initially in aligned states. The results have revealed a strong dependence of specific inelastic cross-sections on the initial alignment. This situation provides another example where one expects that a convincing theoretical model will have to be based on accurate *ab-initio* potential curves and sophisticated treatments of the scattering dynamics.

We consider the process

$$\mathrm{Ca}(4s4f\,{}^1\mathrm{F}) + \mathrm{He} \rightarrow \mathrm{Ca}(4p^2\,{}^1\mathrm{S}) + \mathrm{He}. \tag{23}$$

For this system, Driessen *et al.* (1991a, b) have performed the following experiment. The initial Ca atom is prepared in a well defined state, whose quantization axis is related to the directions of the polarizations of the lasers used to prepare the state. Specifically, ^{1}F states ($J = 3$) whose angular wavefunction is $|J, 0\rangle$ or $[|J, 1\rangle - |J, -1\rangle]/2^{1/2}$ can be prepared. The excited atoms interact with a beam of He atoms incident at an angle β with respect to the quantization axis, and collisions cause transitions to several final Ca states. Transitions to the $4p^2\,{}^1$S are detected by monitoring fluorescence from that state. The experimental signal is the ^{1}S fluorescence as a function of β; this signal is proportional to a cross-section $\sigma(\beta)$ for process (1).

For the conventional analysis of scattering experiments, one usually defines the z axis to coincide with the initial velocity vector of the relative motion. From this point of view, the information contained in $\sigma(\beta)$ could also be expressed as a set of cross-sections σ_M, $M = 0, 1, \ldots, J$, where σ_M is the projection of the initial total atomic angular momentum J on the z axis. (Note that $\sigma_M = \sigma_{-M}$.) The experimental signal $\sigma(\beta)$ is related to the σ_M by

$$\sigma(\beta) = \sum_M \lambda_M(\beta)^2 \sigma_M. \tag{24}$$

The coefficients $\lambda_M(\beta)$ are determined from rotation matrix elements and from the initial state angular wavefunction (Robinson *et al.* 1990). Driessen *et al.* (1991a, b) have given explicit expressions relating $\sigma(\beta)$ to the σ_M for two different arrangements of their laser polarizations. They have measured two sets of σ_M corresponding to two slightly different energy distributions.

The first step of the theoretical analysis was to perform the necessary electronic structure calculations. Figure 13 shows some of the adiabatic potentials, which were calculated (Krebs and Meyer 1993) at the CI level using the core polarization potential of Mueller *et al.* (1984) and a basis set with 15s, 9p, 8d and 5f GTOs. The calculated Ca excitation energies generally agree with experiment within about 150 cm^{-1}, and the spacings between the states near the ^{1}F state are correct to within 20 cm^{-1}. For this system, Krebs and Meyer (1993) calculated radial coupling matrix elements by numerical differentiation. The most important of these couplings are also shown in figure 13. Angular coupling terms (the matrix elements of L_x and L_y) were also calculated.

Analysis of the adiabatic curves in figure 13 indicates two possible transition mechanisms connecting the F and the S levels: radial coupling in the range $(5–8)a_0$ between the two R potentials, and rotational coupling in the same region between the F Π and the S Σ potentials. The latter coupling arises because for R near $6a_0$ or $7a_0$, the adiabatic R state correlating to the ^{1}S asymptote contains some ^{1}F character.

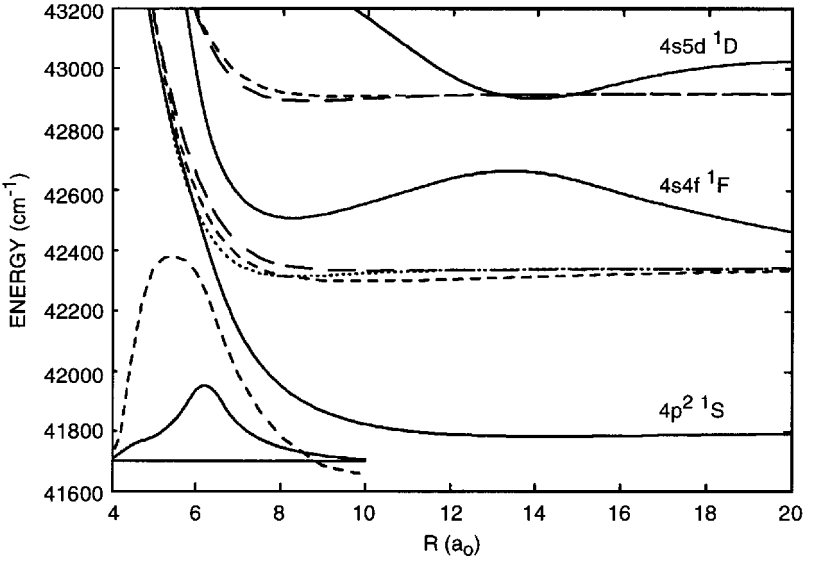

Figure 13. Selected *ab-initio* adiabatic potential curves for CaHe, for Σ (——), Π (– – –), $\triangle$ (— — —) and ϕ (· · ·) symmetry. The inset at lower left shows $\langle \mathrm{F}\,\Pi | L_x | \mathrm{S}\,\Sigma \rangle$ (– – –), which governs the rotational coupling, and the radial coupling term $\langle \mathrm{F}\,\Sigma | \mathrm{d}/\mathrm{d}R | \mathrm{S}\,\Sigma \rangle$ (——).

The scattering equations were solved in the diabatic representation, in order to use existing computer scattering codes. The *ab-initio* calculations of Krebs and Meyer (1993) provided adiabatic potential curves and radial and rotational coupling matrix elements between them. A transformation of the *ab-initio* calculations was implemented by solving the differential equation that related $C(R)$, the transformation between the adiabatic and diabatic representations, to the matrix elements of the $\mathrm{d}/\mathrm{d}R$ operator. One has

$$\frac{\mathrm{d}C^{\mathrm{t}}}{\mathrm{d}R} = P^{\mathrm{t}} C^{\mathrm{t}}, \tag{25}$$

where C is the transformation that diagonalizes the set of $\chi_n(R, \mathbf{r})$ used to define a diabatic representation, thereby providing adiabatic eigenfunctions, and $P(R)_{mn}$ is the radial coupling between adiabatic eigenstates $\chi_m(R, \mathbf{r})$ and $\chi_n(R, \mathbf{r})$ defined in equation (6). Careful attention had to be paid to the diabatization procedure in order to ensure correct signs for the radial coupling terms, since arbitrary sign changes could occur between one value of R and the next.

The cross-sections are defined in terms of the **T** matrix elements, which are determined by solving equation (5) for the appropriate coupling terms. Specifying J and M of the initial Ca state, summing the cross-sections over all projections M' of the final level, and letting α specify all the other quantum numbers, one obtains

$$\sigma_M = \frac{\pi}{k^2} \sum_P (2P+1) \sum_{N'} \left| \sum_N i^N \langle J\,M\,P, -M | N0 \rangle\, T^P_{\alpha' J' N', \alpha J N} \right|^2, \tag{26}$$

where N is the orbital angular momentum of the relative motion of Ca and He, $P = J + N$, and $\langle J\,M\,P, -M | N0 \rangle$ is a Clebsch–Gordan coefficient.

Figure 14 shows the calculated cross-sections σ_M for collision energies

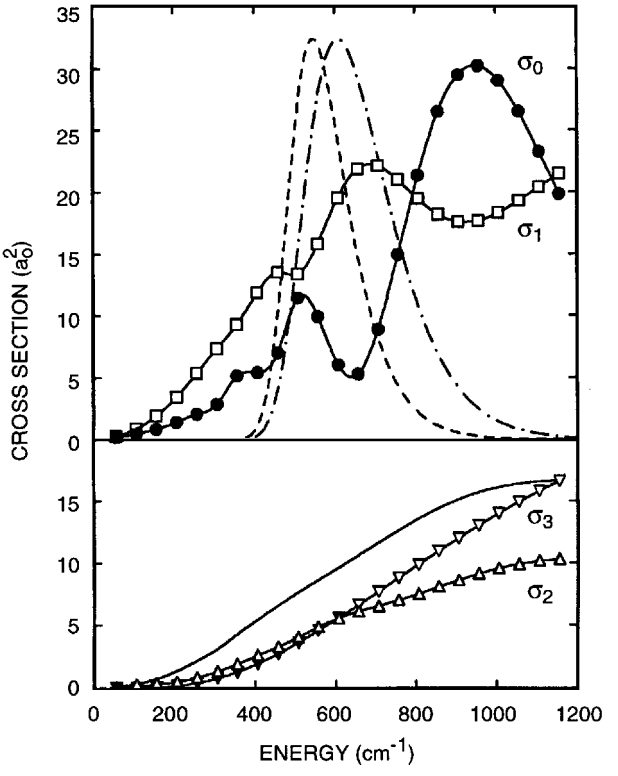

Figure 14. Calculated cross-sections σ_M. (*a*) The collision energy distributions are shown for the initial states $|J,0\rangle$ (– · –) and $(|J,1\rangle - |J,-1\rangle)/2^{1/2}$ (– – –). (*b*) The solid line is the average cross-section.

200–1100 cm^{-1} relative to the initial state $Ca(4s4f\,{}^1F_3)$. The results shown are based on including the F and S levels; additional channels did not change the results significantly. The most striking feature of these results is the strong energy dependence of σ_0 and σ_1, which contrasts with the smooth behaviour of the cross-section averaged over M. The origin of the oscillations is discussed below. We convoluted the cross-sections with the experimental energy distributions (Driessen *et al.* 1991a, b). (We used a peak at 613 cm^{-1} and a full width at half-maximum (FWHM) of 210 cm^{-1} for the $|J,0\rangle$ state and a peak at 540 cm^{-1} and a FWHM of 160 cm^{-1} for the $[|J,1\rangle - |J,-1\rangle]/2^{1/2}$ state.) The convoluted cross-sections are compared with the corresponding experimental values in figure 15. The calculations agree with experiment with respect to the relative size of σ_0 and σ_1, compared with σ_2 and σ_3, but the ordering of σ_0 and σ_1 is reversed. We suspect that this discrepancy is related to the oscillatory behaviour of σ_0 and σ_1, which we interpret as an interference phenomenon depending sensitively on the details of the potentials.

To understand the origin of the oscillations, we examined the collision dynamics in more detail using a semiclassical model. The details of this model have been presented in the literature (Hickman *et al.* 1994). The crucial point is the evolution of the initial states of fixed M in the space-fixed frame into specific molecular states labelled by Λ (Σ, Π, etc.) in the body-fixed frame. For a particular collision with a fixed impact parameter, there is an amplitude for the atoms to 'choose' the Σ or the Π state. For each of these two states, there is a possible mechanism for a transition to the final ^1S

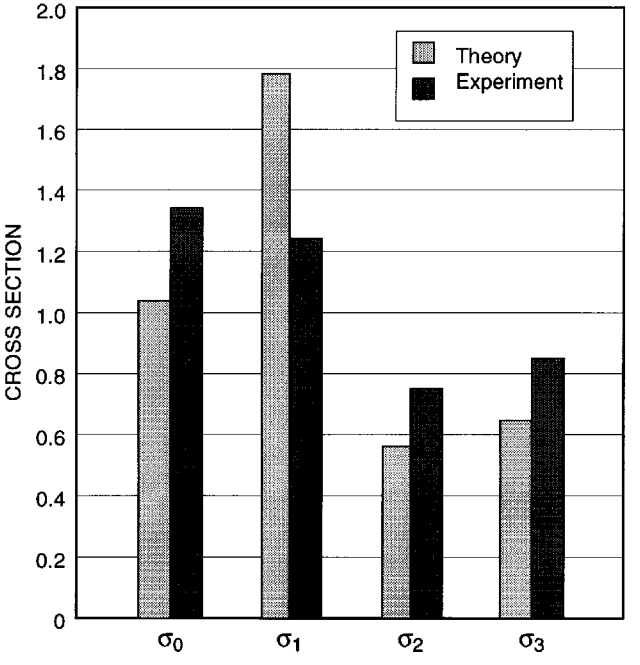

Figure 15. Comparison of energy-averaged cross-sections with experiment (Driessen *et al.* 1991a, b) for the initial state $|J, 0\rangle$.

state. The oscillations in the cross-section arise from the interference between these two alternative mechanisms. The process is analogous to well known curve-crossing models that lead to oscillations in the angular cross-section due to the interference of two possible trajectories that lead to the same scattering angle. What is remarkable in the present case is that the oscillations persist in the total energy, after integrating over the angular cross-section.

The coupled-channel calculations of the partial cross-sections for $M = 0$ to ^{1}S transitions exhibited a complicated oscillatory dependence on energy and impact parameter. As further evidence for the interference effect, we note that suppressing the rotational coupling between the ^{1}F Π curve and the ^{1}S Σ curve eliminates the oscillations in the energy dependence.

The interference effect may also be related to the long-range barrier in the ^{1}F Σ potential shown in figure 13. There is a significant phase difference between trajectories that follow the Σ curve and surmount the barrier, and those that follow the flat Π curve. A model calculation attributing the phase difference to this effect matches the oscillatory behaviour of σ_0 very well. There is another effect of the barrier. At collision energies E less than the barrier height (about 350 cm^{-1}), trajectories that follow the R state will generally not penetrate to the region at small R where transitions to the ^{1}S state can take place. We expect σ_0 to be strongly suppressed then, because the $M = 0$ initial states evolve preferentially into Σ states. Figure 14 confirms that for $E <$ 350 cm^{-1}, σ_1 is the largest partial cross-section, and can be twice to three times larger than the other σ_M. We also note in figure 14 that the oscillations in σ_0 begin at 350–400 cm^{-1}, the energy range at which trajectories that begin in the $M = 0$ state can first surmount the barrier. The quantum-chemical results revealed evidence of orbiting resonances in this energy range.

In conclusion, we have presented a detailed analysis of collisions of aligned Ca(4s4f ^{1}F) atoms with He. The key results are prominent oscillations in the energy dependence of σ_0 and σ_1 and strong enhancement of σ_1 at low collision energies.

5. Concluding remarks

Several methods have been reviewed for implementing coupled-channel calculations of collisions involving electronic excitation processes. The central problem that must be solved to treat these processes is the determination of the appropriate coupling terms between the electronic states. Various methods have been discussed for doing this. For the collisions involving heavy atoms, a sophisticated model for the angular momentum coupling was developed that separated the electronic and spin–orbit terms. The electronic coupling terms were determined from *ab-initio* calculations that invoked effective core potentials to treat inner-shell electrons. Spin–orbit coupling terms of spectroscopic accuracy could also be incorporated in the analysis. For the collisions involving aligned atoms, radial coupling terms were available from *ab-initio* calculations.

Acknowledgments

The work reviewed here was carried out in collaboration with D. L. Huestis, J. J. Portman and R. P. Saxon at SRI International and S. Krebs and W. Meyer at the University of Kasiserlautern. In addition, A.P.H. gratefully acknowledges the support of Sandia National Laboratories, the National Science Foundation, and the Deutsche Forschungsgemeinschaft.

References

Alford, W. J., 1992, *J. chem. Phys.*, **96**, 4330.
Alford, W. J., and Hays, G. N., 1989, *J. appl. Phys.*, **65**, 3760.
Bruce, M. R., Layne, W. B., Whitehead, C. A., and Keto, J. W., 1990, *J. chem. Phys.*, **92**, 2917.
Bussert, W., Neuschaefer, D., and Leone, S. R., 1987, *J. chem. Phys.*, **87**, 3833.
Chang, A. H. H., and Pitzer, R. M., 1989, *J. Am. chem. Soc.*, **111**, 2500.
Cohen, J. S., and Schneider, B. I., 1974, *J. chem. Phys.*, **61**, 3230.
Condon, E. U., and Shortley, G. H., 1967, *The Theory of Atomic Spectra* (Cambridge University Press).
Delos, J. B., 1981, *Rev. mod. Phys.*, **53**, 287.
Driessen, J. P. J., Smith, C. J., and Leone, S. R., 1991a, *Phys. Rev.* A **44**, 1431; 1991b, *J. phys. Chem.*, **95**, 8163.
Gordon, R. G., 1969, *J. chem. Phys.*, **51**, 14.
Hale, M. O., Hertel, I. V., and Leone, S. R., 1984, *Phys. Rev. Lett.*, **53**, 2296.
Hickman, A. P., 1981, *Phys. Rev. Lett.*, **47**, 1585; 1982, *J. Phys.* B, **15**, 3005.
Hickman, A. P., Medikeri-Naphade, M., Chapin, C. D., and Huestis, D. L., 1997, *Geophys. Res. Lett.* **24**, 119.
Hickman, A. P., Portman, J. J., Krebs, S., and Meyer, W., 1994, *Phys. Rev. Lett.*, **72**, 1814.
Hickman, A. P., Saxon, R. P., and Huestis, D. L., 1992, *J. chem. Phys.*, **96**, 2099; 1993, *Ibid.*, **98**, 5419.
Horiguchi, H., Chang, R. S. F., and Setser, D. W., 1981, *J. chem. Phys.*, **75**, 1207.
Inoue, G., Ku, J. K., and Setser, D. W., 1984, *J. chem. Phys.*, **81**, 5760.
Krebs, S., and Meyer, W., 1993, unpublished work.
Lester, W. A., Jr., and Bernstein, R. B., 1968, *J. chem. Phys.*, **48**, 4896.
McQuire, P., and Kouri, D. J., 1974, *J. chem. Phys.*, **60**, 2488.
Moore, C. E., 1958, *Atomic Energy Levels*, Vol. III, National Bureau of Standards, Circular No. 467 (Washington, DC: US Government Printing Office).
Mueller, W., Flesch, J., and Meyer, W., 1984, *J. chem. Phys.*, **80**, 3297.
Nikitin, E. E., 1975, *Adv. chem. Phys.*, **28**, 317.
Ohwa, M. T., Moratz, J., and Kushner, M. J., 1989, *J. appl. Phys.*, **66**, 5131.

PACK, R. T, 1974, *J. chem. Phys.*, **60**, 633.
PITZER, R. M., and WINTER, N. W., 1988, *J. phys. Chem.*, **92**, 3061.
REID, R. H. G., 1973, *J. Phys.* B, **6**, 2018.
ROBINSON, R. L., KOVALENKO, L. J., SMITH, C. J., and LEONE, S. R., 1990, *J. chem. Phys.*, **92**, 5260.
SARAPH, H. E., and SEATON, M. J., 1977, *Phil. Trans. R. Soc.*, **271**, 1.
SECREST, D., 1975, *J. chem. Phys.*, **62**, 710.
SMITH, F. T., 1969, *Phys. Rev.*, **179**, 111.
THORSON, W. R., 1969, *J. chem. Phys.*, **50**, 1702.
WALKER, R. B., and LIGHT, J. C., 1975, *Chem. Phys.*, **7**, 84.
XU, J., and SETSER, D. W., 1990, *J. chem. Phys.*, **92**, 4191.